CONDENSED MATTER PHYSICS

Moiré potential impedes interlayer exciton diffusion in van der Waals heterostructures

Junho Choi¹*, Wei-Ting Hsu¹*, Li-Syuan Lu², Liuyang Sun¹, Hui-Yu Cheng², Ming-Hao Lee³, Jiamin Quan¹, Kha Tran¹, Chun-Yuan Wang^{1,4,5}, Matthew Staab¹, Kayleigh Jones¹, Takashi Taniguchi⁶, Kenji Watanabe⁶, Ming-Wen Chu³, Shangjr Gwo^{4,5}, Suenne Kim⁷, Chih-Kang Shih¹, Xiaoqin Li^{1†}, Wen-Hao Chang^{2,8†}

The properties of van der Waals heterostructures are drastically altered by a tunable moiré superlattice arising from periodically varying atomic alignment between the layers. Exciton diffusion represents an important channel of energy transport in transition metal dichalcogenides (TMDs). While early studies performed on TMD heterobilayers suggested that carriers and excitons exhibit long diffusion, a rich variety of scenarios can exist. In a moiré crystal with a large supercell and deep potential, interlayer excitons may be completely localized. As the moiré period reduces at a larger twist angle, excitons can tunnel between supercells and diffuse over a longer lifetime. The diffusion should be the longest in commensurate heterostructures where the moiré superlattice is completely absent. Here, we experimentally demonstrate the rich phenomena of interlayer exciton diffusion in WSe₂/MoSe₂ heterostructures by comparing several samples prepared with chemical vapor deposition and mechanical stacking with accurately controlled twist angles.

Copyright © 2020 The Authors, some rights reserved; exclusive licensee American Association for the Advancement of Science. No claim to original U.S. Government Works. Distributed under a Creative Commons Attribution NonCommercial License 4.0 (CC BY-NC).

INTRODUCTION

van der Waals (vdW) materials provide exciting opportunities to create new heterostructures with vastly expanded choices of materials, as the strict requirement of lattice matching between adjacent layers has been lifted (1). Most intriguingly, a moiré superlattice emerges because of the periodic variations in atomic alignment between adjacent layers. The period of the moiré superlattice can be readily controlled by choosing materials with different lattice constants or adjusting the twist angle between the layers, leading to a new paradigm in engineering quantum materials (2–4). For example, graphene bilayers can exhibit either superconducting or insulating phases driven by electron correlation controllable via the twist angle (5–8). Such a strategy has yet to be carefully explored in controlling semiconductor heterostructures built with transition metal dichalcogenides (TMDs) (9, 10).

A type II band alignment is typically found in a TMD heterobilayer (hBL), leading to rapid electron transfer to one layer and hole transfer to the other layer and the formation of interlayer excitons (IXs) (11–13). These IX resonances are the lowest energy optical excitations and shifted from the intralayer excitons mainly by the band alignments (14–19). The diffusion and mobility of various carriers including electrons, holes, and IXs are important properties because they determine the charge and energy transport processes in hBLs, which, in turn, are critical for building transistors and photovoltaic

devices. Several experiments performed on WS₂/WSe₂, MoS₂/WSe₂, and MoSe₂/WSe₂ hBLs have reported long free carrier and IX diffusion length and electric field control of this transport (*16*, *17*, *20*–*22*). Other recent experiments, on the other hand, suggest that IXs may be localized by the moiré potential on the order of 100 to 200 meV (*18*, *19*, *23*). These seemingly conflicting results suggest rich opportunities to control the optical properties of TMD heterostructures.

Here, we investigate the influence of the moiré potential on IX diffusion in WSe₂/MoSe₂ hBLs using spatially and time-resolved photoluminescence (PL) measurements. We carefully compare experiments performed on two types of samples either grown by chemical vapor deposition (CVD) or created by the mechanical exfoliation and transfer (MET) with a well-controlled twist angle. IX diffusion length in the rotationally aligned CVD-grown hBL exceeds the size of the hBL and is estimated to be a few microns. In contrast, no IX diffusion beyond the excitation laser spot is observed in the stacked hBL with ~1° twist angle, suggesting that IXs may be localized by the moiré potential. In another MET sample with ~3.5° twist angle, IX diffusion is observed but with a short diffusion length of \sim 1 μm despite nearly ~100-fold longer lifetime than that in the CVD-grown sample. These experiments suggest that IX diffusion is highly controllable via engineering the moiré superlattice and provides valuable guidance to extensive effort in searching for IX Bose-Einstein condensate (BEC) (24, 25) or localized quantum emitters in the TMD heterostructures (3, 4, 18, 19, 26, 27).

¹Department of Physics, Complex Quantum Systems, and Texas Materials Institute, The University of Texas at Austin, Austin, TX 78712, USA. ²Department of Electrophysics, National Chiao Tung University, Hsinchu 30010, Taiwan. ³Center for Condensed Matter Sciences, National Taiwan University, Taipei 10617, Taiwan. ⁴Department of Physics, National Tsing-Hua University, Hsinchu 30013, Taiwan. ⁵Research Center for Applied Sciences, Academia Sinica, Nankang, Taipei 11529, Taiwan. ⁶National Institute for Materials Science, 1-1 Namiki, Tsukuba, Ibaraki 305-0044, Japan. ⁷Department of Photonics and Nanoelectronics, Hanyang University, Ansan 15588, Republic of Korea. ⁸Center for Emergent Functional Matter Science (CEFMS), National Chiao Tung University, Hsinchu 30010, Taiwan.

RESULTS

We briefly describe the samples investigated here. We focus on WSe₂/MoSe₂ hBLs with R-stacking style or near this stacking style, where a deep moiré potential is expected (28, 29). The stacking style is confirmed by transmission electron microscope (TEM) images or second harmonic generation (SHG) (see the Supplementary Materials). The optical microscope images and structural illustrations for the CVD (sample A) and MET (samples B and C) methods are shown in Fig. 1 (A, B, D, and E, respectively). The lattice constants

^{*}These authors contributed equally to this work.

 $[\]label{thm:corresponding} \begin{tabular}{ll} $\mbox{$+$ Corresponding author. Email: elaineli@physics.utexas.edu (X.L.); whchang@mail. nctu.edu.tw (W.-H.C.) \end{tabular}$

of MoSe₂ and WSe₂ are very close to each other. In samples A-1 and A-2 grown by the CVD method, the lattice in each layer is slightly distorted to form a commensurate and rotationally aligned (i.e., 0° twist angle) hBL as illustrated in Fig. 1C. The hBL regions are limited to the bright inner triangle with a typical lateral size of $\sim 10 \ \mu m$ (Fig. 1A). In the MET samples, a twist angle $\theta = 1.1^{\circ} \pm 0.3^{\circ}$ (sample B-1), $\theta = 1.3^{\circ} \pm 0.3^{\circ}$ (sample B-2), and $\theta = 3.5^{\circ} \pm 0.3^{\circ}$ (sample C) from the R-stacking leads to the formation of a moiré superlattice (Fig. 1F). The twist angle is determined from a high-resolution optical image, SHG (see the Supplementary Materials), and further confirmed by IX lifetime measurements presented later. The presence of the moiré potential and its periodicity plays a major role in determining exciton diffusion as illustrated in Fig. 1 (C and F) and demonstrated in the rest of the paper. Both intralayer excitons and IXs are observed (PL spectra included in the Supplementary Materials), while we focus on the properties of the IXs in this paper.

IX diffusion is investigated using spatially and spectrally resolved PL in all samples as shown in Fig. 2 (A to F). We examine the spatial PL line profiles at a few selected energies at the center, lower, and higher energy side of the broad IX spectral feature. No pronounced energy dependence is observed in any of these samples. However, the spatial IX diffusion is remarkably different between these samples. The diffusion lengths in the CVD samples A-1 and A-2 are the longest and limited by the physical size of the hBL region. In contrast, no IX diffusion beyond the excitation laser spot size is observed in the MET samples B-1 and B-2 with $\theta = \sim 1^{\circ}$. The full width at half maximum (FWHM) of a Gaussian function fitted to the excitation laser spot yields $\sim 1 \mu m$. The size of the IX PL spot appears slightly larger than the excitation laser spot size in Fig. 2E, which is caused by the imaging optics (e.g., microscope objective and curved mirrors inside the spectrograph) at different wavelengths (i.e., IXs near 900 nm and the excitation laser at 660 nm). Interestingly, the IX diffusion is found to depend on the moiré period and the IX lifetimes. When the moiré period is reduced from

20 nm in sample B-1 to 5.7 nm in another MET sample C with $\theta = \sim 3.5^{\circ}$, IX diffusion beyond the excitation spot size becomes observable as shown in Fig. 2 (C and F).

IX diffusion can be quantitatively analyzed using the following equation (30, 31)

$$\frac{\partial n(r,t)}{\partial t} = -\nabla \cdot \left(-D_{\text{IX}} \nabla n(r,t) - n(r,t) \mu u_0 \nabla n(r,t) \right)
- \frac{n(r,t)}{\tau_{\text{IX}}} + G(r,t)$$
(1)

where n(r, t) is the IX density, $D_{\rm IX}$ is the diffusion coefficient, μ is the exciton mobility, u_0 is the IX interaction energy, $\tau_{\rm IX}$ is the IX lifetime, and G(r, t) is the exciton generation term, respectively (more details in the Supplementary Materials). To avoid the complications arising from exciton-exciton annihilation and repulsive interaction at high excitation density (20, 32, 33), all experiments presented here are performed at a low excitation power of 1 μ W, corresponding to an estimated IX density of ~10 9 /cm 2 . We present the power-dependent studies for all three samples in the Supplementary Materials. Making the assumption that the interaction effect can be neglected at low density, the steady-state IX density follows the analytical solution (32)

$$n(r) \propto \int_{-\infty}^{\infty} K_0\left(\frac{r}{L_{\rm IX}}\right) e^{-(r-r')^2/w^2} dr'$$
 (2)

This solution is a convolution between the Gaussian profile of incident laser and the modified Bessel function of the second kind K_0 with the diffusion length $L_{\rm IX} = \sqrt{D_{\rm IX}}\tau_{\rm IX}$, where $\tau_{\rm IX}$ and $D_{\rm IX}$ are the IX lifetime and diffusion coefficient, respectively. A series of solutions are generated by varying $L_{\rm IX}$ as shown in Fig. 3A. Comparing the 1/e width of the simulated curves and the experimental data, we extracted a range of diffusion lengths for CVD sample A-1 (A-2) to be 3 to 16 (2.4 to 13.5) μ m and for sample C to be ~1 μ m. The uncertainty in diffusion lengths in CVD-grown samples partially

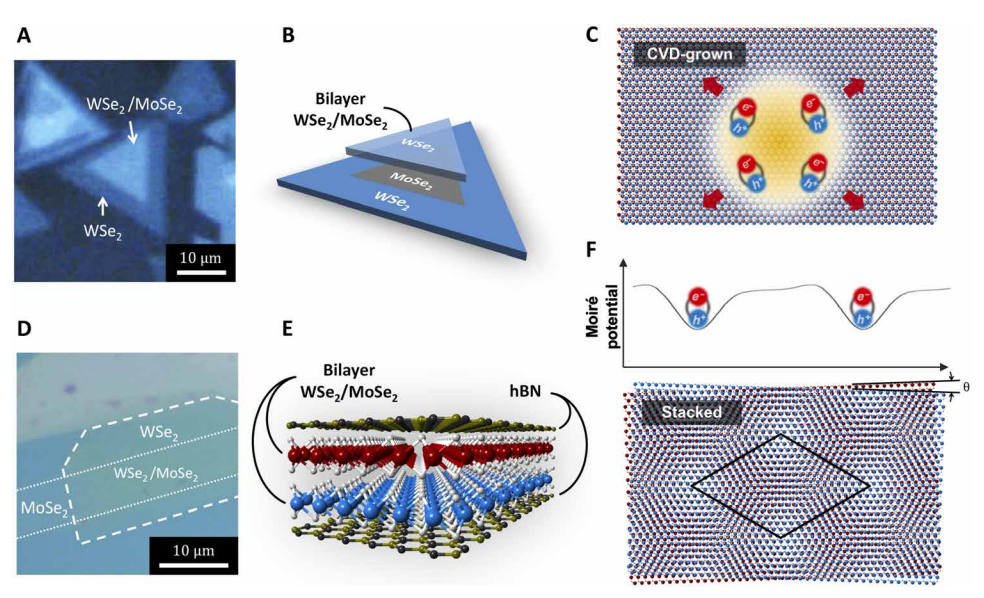


Fig. 1. Two types of WSe₂/MoSe₂ heterostructures and the absence/presence of moiré superlattice. (A) Optical images of CVD-grown sample A-1. (B) Illustrated CVD-grown hBL, which consists of a monolayer WSe₂ covering on top of a monolayer MoSe₂-WSe₂ lateral heterostructure. (C) Schematics of exciton diffusion in a CVD-grown WSe₂/MoSe₂ bilayer with a commensurate structure. (D) Optical image of mechanically stacked WSe₂/MoSe₂ hBL sample B-1. (E) Illustration of the hBN-encapsulated WSe₂/MoSe₂ hBL. (F) impeded exciton diffusion by the moiré potential in a MET hBL. The moiré supercell size decreases with an increasing twist angle θ between the two layers.

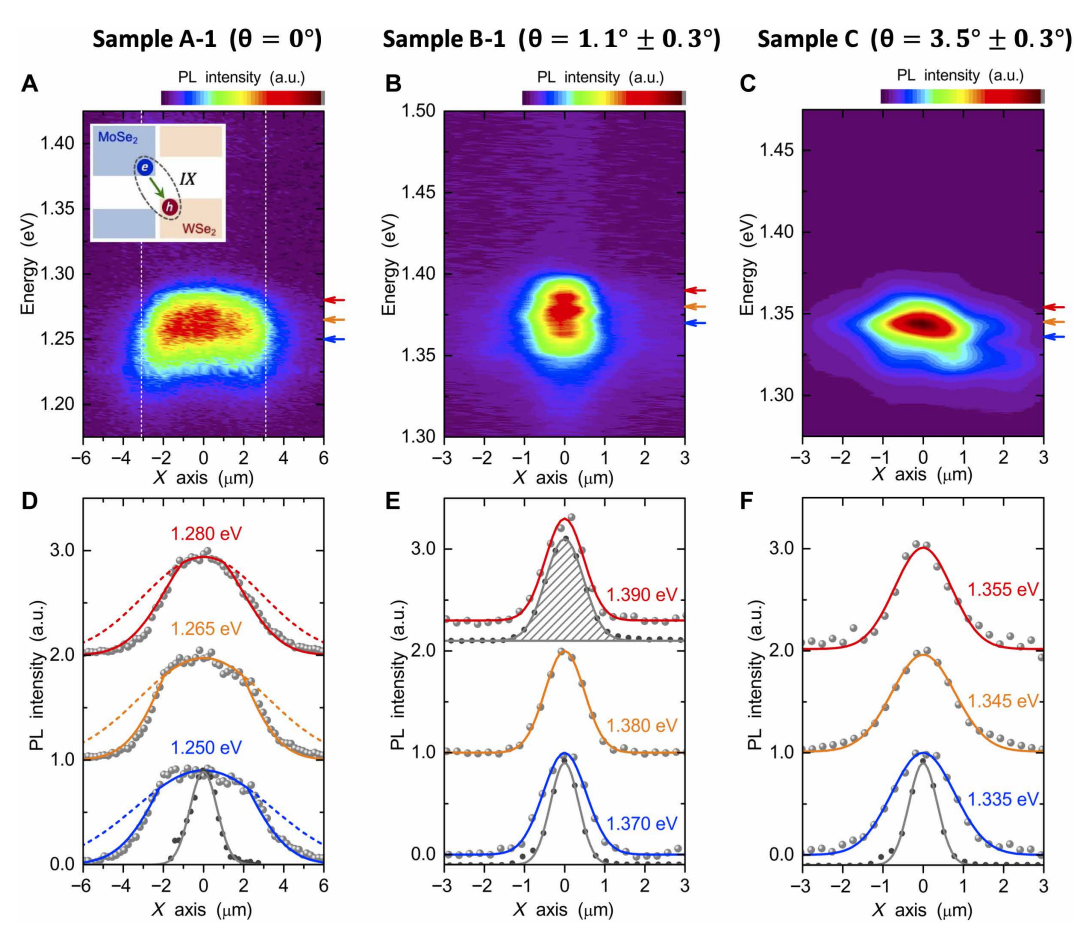


Fig. 2. Spatially resolved PL images. Two-dimensional PL images and spectra of the IXs with the spatial (energy) coordinate were shown in the horizontal (vertical) axis for **(A)** CVD-grown sample A-1, **(B)** MET sample B-1 with $\theta = 1.1^{\circ} \pm 0.3^{\circ}$, and **(C)** MET sample C with $\theta = 3.5^{\circ} \pm 0.3^{\circ}$. A much longer IX diffusion length in sample A-1 is clearly observed. The corresponding PL line profiles were taken from **(D)** sample A-1, **(E)** sample B-1, and **(F)** sample C, respectively. Note that the PL profiles from sample A-1 are truncated by the boundaries of the hBL region as indicated by the white dashed lines in (A). In addition, line profiles of excitation laser spots (bottom gray lines) are displayed. The 900-nm laser profile (top gray shaded) is displayed in (E) to illustrate that the PL image is limited by excitation spot size and imaging optics in sample B-1. Measured data points are fitted by a Gaussian function. a.u., arbitrary units.

arises from the truncated data due to the limited size of the flake. We used several different models to analyze $L_{\rm IX}$ and the range of values as shown in Fig. 3B (see the Supplementary Materials for more details).

We further analyze the diffusion coefficients of IXs by measuring IX lifetimes using time-resolved PL (TRPL) measurements. The data in Fig. 3C are fitted with either a biexponential or single-exponential decay function, and extracted lifetimes are shown in Fig. 3D. In sample A-1 (A-2), a biexponential fit leads to a fast and slow component of $\tau_1^A = 1.2$ (1.0) ns and $\tau_2^A = 5.5$ (5.9) ns and a weighted average lifetime of 1.7 (1.8) ns. This IX lifetime is similar to $\tau^B = \sim 1$ ns for samples B-1 and B-2 but markedly different from $\tau^{C} = \sim 100$ ns for sample C. The lifetimes measured from both types of hBLs are consistent with the previous experiments (14, 19, 34, 35). The remarkably longer lifetime found in sample C is related to the momentum space shift between the conduction and valence bands in twisted bilayers, leading to an indirect transition in both real and momentum space (36). This angle-dependent lifetime is confirmed in many of our hBLs prepared by the MET method. Using $D_{\rm IX} = L_{\rm IX}^2/\tau_{\rm IX}$, an effective diffusion coefficient is estimated to be ~50 (30) cm²/s for sample A-1 (A-2), larger than the typical value reported for incommensurate hBLs (16, 20, 21). The extracted value for sample C is $\sim 0.1 \text{ cm}^2/\text{s}$, consistent with previous studies (see the Supplementary Materials for details).

The absence of the moiré pattern in sample A is directly proven by a high-resolution scanning TEM (STEM) image as shown in Fig. 4A. The brightest points identify the positions of Mo atoms, the second brightest points correspond to W atoms, and the dimmest ones are from the Se atoms. The commensurate atomic registry is proven by the uniform pattern observed in the STEM image. The schematic in Fig. 4B illustrates the 3R-like stacking of this atomic registry, in which the Se atoms are directly positioned on top of the Mo atoms. A MET hBL cannot be easily transferred and identified on a standard TEM grid. Thus, we perform atomic force microscopy (AFM) measurements to examine the atomic alignment in a mechanically stacked hBL. We follow the same procedure to prepare a sample without the top hexagonal boron nitride (hBN) to expose the WSe₂/MoSe₂ hBL, which enables AFM imaging (see Materials and Methods for details). Despite some contaminants on the sample, we observe a disordered hexagonal pattern with a period of ~20 nm, suggesting a small twist angle of ~1° in this particular sample (Fig. 4C).

DISCUSSION

Recognizing that the quality of hBLs can vary, we repeated these measurements on different samples and on different locations of the same sample (more data in the Supplementary Materials). All experiments yielded consistent observations. The longest diffusion length is always observed in the CVD-grown commensurate WSe₂/ MoSe₂ hBLs. A finite diffusion length of ~1 µm is observed in a stacked

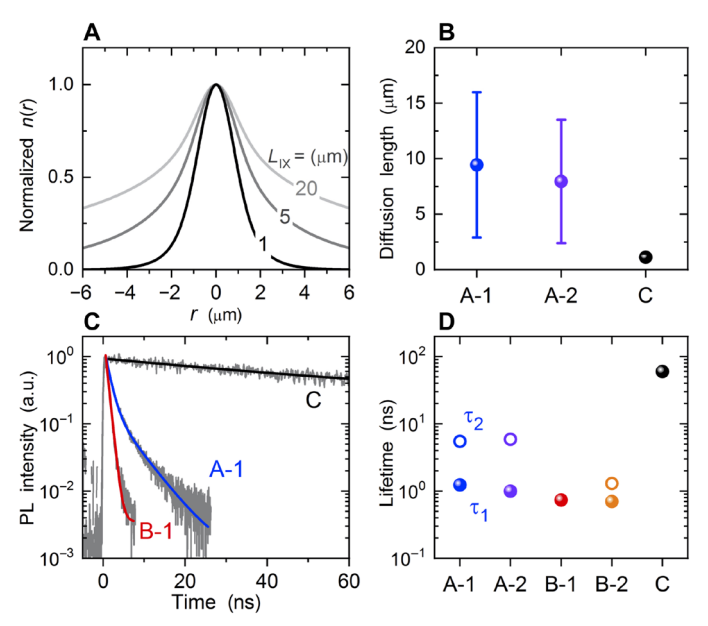


Fig. 3. Determination of IXs diffusion length ($L_{\rm IX}$) **and measured IX lifetimes.** (**A**) Calculated spatial distribution of IX density, in which n(r) is convoluted by the Gaussian laser profile with ~1- μ m FWHM spot size. The measurements are compared to the simulated density distribution function to obtain the diffusion length for each sample. (**B**) IX diffusion length $L_{\rm IX}$ from samples A-1, A-2, and C. (**C**) Timeresolved PL (TRPL) spectra from samples A-1, B-1, and C, respectively. The TRPL spectrum was taken at the center of the IX resonances. The TRPL spectrum is fitted by a single- or double-exponential decay function. The lifetimes extracted from fittings are summarized in (**D**) for all five samples. Note that the error bars of lifetimes are smaller than the dots.

hBL with a relatively large twist angle, while no diffusion beyond the laser spot is observed in stacked hBLs with a small twist angle $(\theta = \sim 1^{\circ})$.

The strikingly different IX diffusion in CVD and MET hBLs is most naturally explained by taking into account the absence/presence of the moiré potential. While there are other differences between CVD-grown and MET hBLs—e.g., substrates, defect density, and interface quality—these differences cannot account for the different IX diffusions and the controllable changes on the stacked samples. The CVD samples are not grown on an atomically smooth substrate and likely exhibit higher defect density. Both factors should lead to a shorter diffusion length than the MET samples (33). Furthermore, the notably longer IX lifetime in the stacked hBL with $\theta = \sim 3.5^{\circ}$ (sample C) should lead to a longer diffusion length than the CVD sample A if their diffusion coefficients were similar.

The difference between two MET hBLs arises from the expected changes in moiré periods and measured exciton lifetimes. For a moiré crystal with a small periodicity, excitons may tunnel between different supercells, and diffusion is observable over a long IX lifetime. For a moiré crystal with a relatively large periodicity, the tunneling between different supercells is exponentially reduced. IXs become localized within a moiré supercell due to a reduced lifetime and decreased velocity. Our conclusion is qualitatively consistent with previous experiments (16, 17, 20, 21) that reported finite IX or carrier diffusion in hBLs with a small moiré period in the sense exciton diffusion beyond the diffraction limit can be observed. Although some quantitative variations in diffusion lengths and diffusion coefficients exist in the literature, they mostly arise from the different diffusion models and analysis (see the Supplementary Materials) and, to a less extent, the preparation procedure of MET bilayers. To establish a more detailed correlation between the moiré supercell size and exciton diffusion, future experimental techniques with higher spatial and/or temporal resolutions are required.

Moiré potential has been demonstrated to have a profound influence on the electronic and optical properties of vdW heterostructures. However, its role in exciton diffusion has been largely ignored in previous studies on hBLs consisting of TMD monolayers with rather different lattice constants or with larger twist angles (16, 17, 20).

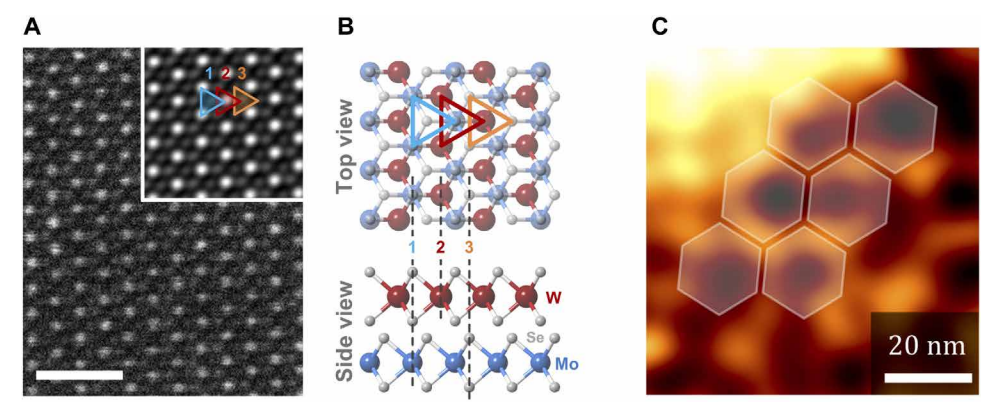


Fig. 4. Crystal structures of CVD-grown and MET hBLs. (A) A STEM image of a CVD-grown hBL similar to sample A shows a commensurate atomic registry, where the Bragg-filtered image is shown in the inset for comparison. Scale bar, 1 nm. (**B**) Schematic showing the ideal atomic registry with top (side) view in the top (bottom) panel. The STEM contrast originates from the difference of total atomic number in each atomic column. The different atomic columns are indicated by black dashed lines: column 1, one Mo atom and two Se atoms (blue triangle); column 2, one W atom (red triangle); column 3, two Se atoms (orange triangle). (**C**) Filtered AFM phase image of an hBL prepared similar to samples B and C, showing a hexagonal pattern consistent with the moiré superlattice. The bright spots at the upper left corner are from surface contaminations.

Our experiments present a complementary view of IX diffusion from previous studies and highlight the influence of the moiré potential on exciton diffusion in hBLs. These studies provide critical guidance for intensive efforts on searching for IX BEC or quantum emitters in TMD heterostructures. IX BEC only occurs when the exciton density exceeds a threshold value. In this case, mobile excitons are preferred and are more likely found in either CVD-grown samples or MET samples with small moiré periods. On the other hand, localized excitons leading to a regular array of quantum emitters are more likely hosted in stacked hBLs with a small twist angle and large moiré period.

MATERIALS AND METHODS

Optical measurements

For the CVD-grown sample A, PL measurements were taken at $T=4~\rm K$ inside a cryogen-free low-vibration cryostat equipped with a three-axis piezo-positioner and an objective lens (numerical aperture, 0.82) mounted inside the cryostat. The excitation sources at 632 nm (750 nm) were provided by a He-Ne (continuous wave Ti: Sapphire) laser. The PL signal was then sent to a 0.75-m monochromator and detected by a nitrogen-cooled charge-coupled device camera. For TRPL measurements, a 635-nm pulsed laser diode (~90-ps width and 40-MHz repetition rate) was used as the excitation source, and the PL was detected by a fast avalanche diode. The PL decays were recorded using the time-correlated single-photon counting technique with a temporal resolution of ~100 ps. Slightly different experimental conditions for measurements performed on samples B and C can be found in the Supplementary Materials.

CVD growth process and STEM characterizations

Single-crystal WSe₂/MoSe₂ hBLs were grown on sapphire substrates by CVD following a previously developed one-step growth process (37, 38). High-purity MoO₂ (99%; Sigma-Aldrich), WO₃, and Se powders (99.5%; Alfa Aesar) were used as the initial reactants. The hBLs were grown at 880°C in H₂/Ar flowing gas at low pressure (5 to 40 torr). During the growth, the flow rates for H₂/Ar gas were set to 6/60 standard cubic centimeters per minute. For STEM measurements, the samples were capped with poly(methylmethacrylate) (PMMA) (950K A4) by spin-coating and then baked at 100°C for 60 min. The WSe₂/MoSe₂ hBLs were then transferred onto a TEM grid by PMMA-based wet transfer procedures. Annular dark-field STEM images were obtained using a spherical aberration-corrected TEM (JEOL-2100F). The detailed growth and characterization processes can be found in (29).

AFM measurements

We obtained the phase image using the tapping mode of AFM (NX10, Park Systems) with a conductive cantilever (PPP-EFM) at \sim 28°C and \sim 68% relative humidity. To obtain the image, the tip was brought to the sample as close as possible, i.e., if the setpoint was lowered further, then a large oscillating noise appeared due to the tip-sample interaction. The hexagonal pattern was only observable in selected areas of the sample due to surface contaminants. The inverse fast Fourier transform of an AFM phase image was obtained using XEI (Park Systems) software.

Mechanically stacked bilayer preparation

The MoSe₂, WSe₂ monolayers (2D semiconductors), and the top hBN capping layer were mechanically exfoliated onto a polydimeth-

ylsiloxane (PDMS) sheet. The bottom hBN layer was directly exfoliated onto a SiO_2/Si substrate. The crystal orientations of $MoSe_2$ and WSe_2 monolayers were identified by polarization-resolved SHG. Using a hemisphere PDMS dot with polycarbonate (PC) film-based dry-transfer technique (39), the top hBN layer was picked up and used to stack the $MoSe_2$ and WSe_2 bilayer by picking up each layer sequentially. The rotational alignment of the crystal orientations of the monolayers was guided by high-resolution optical microscope images. The stacked hBN/ $MoSe_2/WSe_2$ layers were transferred on the bottom hBN layer, and then the heterostructure was dipped in an acetone bath to clean off PC residue. Thermal annealing in a high vacuum ($\sim 10^{-7}$ mbar) at 200°C for 4 hours was performed to improve the interfaces. Polarization-resolved SHG measurements on the heterostructure region were performed to confirm the twist angle and distinguish between R- and H-stacking orders (40).

SUPPLEMENTARY MATERIALS

Supplementary material for this article is available at http://advances.sciencemag.org/cgi/content/full/6/39/eaba8866/DC1

REFERENCES AND NOTES

- Y. Liu, N. O. Weiss, X. Duan, H.-C. Cheng, Y. Huang, X. Duan, van der Waals heterostructures and devices. Nat. Rev. Mater. 1, 16042 (2016).
- F. Wu, T. Lovorn, A. H. MacDonald, Topological exciton bands in moiré heterojunctions. Phys. Rev. Lett. 118, 147401 (2017).
- F. C. Wu, T. Lovorn, A. H. MacDonald, Theory of optical absorption by interlayer excitons in transition metal dichalcogenide heterobilayers. *Phys. Rev. B* 97, 035306 (2018).
- H. Yu, G.-B. Liu, J. Tang, X. Xu, W. Yao, Moiré excitons: From programmable quantum emitter arrays to spin-orbit–coupled artificial lattices. Sci. Adv. 3, e1701696 (2017).
- Y. Cao, V. Fatemi, S. Fang, K. Watanabe, T. Taniguchi, E. Kaxiras, P. Jarillo-Herrero, Unconventional superconductivity in magic-angle graphene superlattices. *Nature* 556, 43–50 (2018)
- Y. Cao, V. Fatemi, A. Demir, S. Fang, S. L. Tomarken, J. Y. Luo, J. D. Sanchez-Yamagishi, K. Watanabe, T. Taniguchi, E. Kaxiras, R. C. Ashoori, P. Jarillo-Herrero, Correlated insulator behaviour at half-filling in magic-angle graphene superlattices. *Nature* 556, 80–84 (2018).
- C. R. Dean, L. Wang, P. Maher, C. Forsythe, F. Ghahari, Y. Gao, J. Katoch, M. Ishigami, P. Moon, M. Koshino, T. Taniguchi, K. Watanabe, K. L. Shepard, J. Hone, P. Kim, Hofstadter's butterfly and the fractal quantum Hall effect in moiré superlattices. *Nature* 497, 598–602 (2013).
- K. Kim, A. DaSilva, S. Huang, B. Fallahazad, S. Larentis, T. Taniguchi, K. Watanabe,
 B. J. LeRoy, A. H. MacDonald, E. Tutuc, Tunable moiré bands and strong correlations in small-twist-angle bilayer graphene. *Proc. Natl. Acad. Sci. U.S.A.* 114, 3364–3369 (2017).
- D. Costanzo, S. Jo, H. Berger, A. F. Morpurgo, Gate-induced superconductivity in atomically thin MoS₂ crystals. *Nat. Nanotechnol.* 11, 339–344 (2016).
- J. Lu, O. Zheliuk, Q. Chen, I. Leermakers, N. E. Hussey, U. Zeitler, J. Ye, Full superconducting dome of strong Ising protection in gated monolayer WS₂. Proc. Natl. Acad. Sci. U.S.A. 115, 3551–3556 (2018).
- M.-H. Chiu, C. Zhang, H.-W. Shiu, C.-P. Chuu, C.-H. Chen, C.-Y. S. Chang, C.-H. Chen, M.-Y. Chou, C.-K. Shih, L.-J. Li, Determination of band alignment in the single-layer MoS₂/ WSe, heterojunction. *Nat. Commun.* 6, 7666 (2015).
- J. Kang, S. Tongay, J. Zhou, J. Li, J. Wu, Band offsets and heterostructures of twodimensional semiconductors. *Appl. Phys. Lett.* 102, 012111 (2013).
- K. Kośmider, J. Fernández-Rossier, Electronic properties of the MoS₂-WS₂ heterojunction. Phys. Rev. B 87, 075451 (2013).
- P. Rivera, J. R. Schaibley, A. M. Jones, J. S. Ross, S. Wu, G. Aivazian, P. Klement, K. Seyler, G. Clark, N. J. Ghimire, J. Yan, D. G. Mandrus, W. Yao, X. Xu, Observation of long-lived interlayer excitons in monolayer MoSe₂-WSe₂ heterostructures. *Nat. Commun.* 6, 6242 (2015).
- Y. Gong, J. Lin, X. Wang, G. Shi, S. Lei, Z. Lin, X. Zou, G. Ye, R. Vajtai, B. I. Yakobson, H. Terrones, M. Terrones, B. K. Tay, J. Lou, S. T. Pantelides, Z. Liu, W. Zhou, P. M. Ajayan, Vertical and in-plane heterostructures from WS₂/MoS₂ monolayers. *Nat. Mater.* 13, 1135–1142 (2014).
- P. Rivera, K. L. Seyler, H. Yu, J. R. Schaibley, J. Yan, D. G. Mandrus, W. Yao, X. Xu, Valley-polarized exciton dynamics in a 2D semiconductor heterostructure. *Science* 351, 688–691 (2016)
- D. Unuchek, A. Ciarrocchi, A. Avsar, K. Watanabe, T. Taniguchi, A. Kis, Room-temperature electrical control of exciton flux in a van der Waals heterostructure. *Nature* 560, 340–344 (2018).

SCIENCE ADVANCES | RESEARCH ARTICLE

- K. L. Seyler, P. Rivera, H. Yu, N. P. Wilson, E. L. Ray, D. G. Mandrus, J. Yan, W. Yao, X. Xu, Signatures of moiré-trapped valley excitons in MoSe₂/WSe₂ heterobilayers. *Nature* 567, 66–70 (2019).
- K. Tran, G. Moody, F. Wu, X. Lu, J. Choi, K. Kim, A. Rai, D. A. Sanchez, J. Quan, A. Singh, J. Embley, A. Zepeda, M. Campbell, T. Autry, T. Taniguchi, K. Watanabe, N. Lu, S. K. Banerjee, K. L. Silverman, S. Kim, E. Tutuc, L. Yang, A. H. MacDonald, X. Li, Evidence for moiré excitons in van der Waals heterostructures. *Nature* 567, 71–75 (2019).
- L. A. Jauregui, A. Y. Joe, K. Pistunova, D. S. Wild, A. A. High, Y. Zhou, G. Scuri, K. De Greve, A. Sushko, C.-H. Yu, T. Taniguchi, K. Watanabe, D. J. Needleman, M. D. Lukin, H. Park, P. Kim, Electrical control of interlayer exciton dynamics in atomically thin heterostructures. *Science* 366, 870–875 (2019).
- C. Jin, J. Kim, M. I. B. Utama, E. C. Regan, H. Kleemann, H. Cai, Y. Shen, M. J. Shinner, A. Sengupta, K. Watanabe, T. Taniguchi, S. Tongay, A. Zettl, F. Wang, Imaging of pure spin-valley diffusion current in WS₂-WSe₂ heterostructures. Science 360, 893–896 (2018).
- D. Unuchek, A. Ciarrocchi, A. Avsar, Z. Sun, K. Watanabe, T. Taniguchi, A. Kis, Valley-polarized exciton currents in a van der Waals heterostructure. *Nat. Nanotechnol.* 14, 1104–1109 (2019)
- L. Yuan, B. Zheng, J. Kunstmann, T. Brumme, A. B. Kuc, C. Ma, S. Deng, D. Blach, A. Pan,
 L. Huang, Anomalous interlayer exciton diffusion in twist-angle-dependent moiré potentials of WS₂-WSe₂ heterobilayers. arXiv:1910.02869 [cond-mat.mtrl-sci] (2019).
- M. M. Fogler, L. V. Butov, K. S. Novoselov, High-temperature superfluidity with indirect excitons in van der Waals heterostructures. *Nat. Commun.* 5, 4555 (2014).
- F.-C. Wu, F. Xue, A. H. MacDonald, Theory of two-dimensional spatially indirect equilibrium exciton condensates. *Phys. Rev. B* 92, 165121 (2015).
- C. Jin, E. C. Regan, A. Yan, M. I. B. Utama, D. Wang, S. Zhao, Y. Qin, S. Yang, Z. Zheng, S. Shi, K. Watanabe, T. Taniguchi, S. Tongay, A. Zettl, F. Wang, Observation of moiré excitons in WSe₂/WS₂ heterostructure superlattices. *Nature* 567, 76–80 (2019).
- N. Zhang, A. Surrente, M. Baranowski, D. K. Maude, P. Gant, A. Castellanos-Gomez, P. Plochocka, Moiré intralayer excitons in a MoSe₂/MoS₂ heterostructure. *Nano Lett.* 18, 7651–7657 (2018).
- 28. C. Zhang, C.-P. Chuu, X. Ren, M.-Y. Li, L.-J. Li, C. Jin, M.-Y. Chou, C.-K. Shih, Interlayer couplings, Moiré patterns, and 2D electronic superlattices in MoS₂/WSe₂ hetero-bilayers. *Sci. Adv.* **3**, e1601459 (2017).
- W.-T. Hsu, L.-S. Lu, P.-H. Wu, M.-H. Lee, P.-J. Chen, P.-Y. Wu, Y.-C. Chou, H.-T. Jeng, L.-J. Li, M.-W. Chu, W.-H. Chang, Negative circular polarization emissions from WSe₂/MoSe₂ commensurate heterobilayers. *Nat. Commun.* 9, 1356 (2018).
- A. L. Ivanov, Quantum diffusion of dipole-oriented indirect excitons in coupled quantum wells. Europhys. Lett. 59, 586–591 (2002).
- R. Rapaport, G. Chen, S. H. Simon, Nonlinear dynamics of a dense two-dimensional dipolar exciton gas. *Phys. Rev. B* 73, 033319 (2006).
- F. Cadiz, C. Robert, E. Courtade, M. Manca, L. Martinelli, T. Taniguchi, K. Watanabe, T. Amand, A. C. H. Rowe, D. Paget, B. Urbaszek, X. Marie, Exciton diffusion in WSe₂ monolayers embedded in a van der Waals heterostructure. *Appl. Phys. Lett.* 112, 152106 (2018).
- L. Yuan, T. Wang, T. Zhu, M. Zhou, L. Huang, Exciton dynamics, transport, and annihilation in atomically thin two-dimensional semiconductors. J. Phys. Chem. Lett. 8, 3371–3379 (2017).
- P. Nagler, M. V. Ballottin, A. A. Mitioglu, F. Mooshammer, N. Paradiso, C. Strunk, R. Huber, A. Chernikov, P. C. M. Christianen, C. Schüller, T. Korn, Giant magnetic splitting inducing near-unity valley polarization in van der Waals heterostructures. *Nat. Commun.* 8, 1551 (2017).
- B. Miller, A. Steinhoff, B. Pano, J. Klein, F. Jahnke, A. Holleitner, U. Wurstbauer, Long-Lived Direct and Indirect Interlayer Excitons in van der Waals Heterostructures. *Nano Lett.* 17, 5229–5237 (2017).
- H. Yu, Y. Wang, Q. Tong, X. Xu, W. Yao, Anomalous light cones and valley optical selection rules of interlayer excitons in twisted heterobilayers. *Phys. Rev. Lett.* 115, 187002 (2015).
- Y.-H. Chang, W. Zhang, Y. Zhu, Y. Han, J. Pu, J.-K. Chang, W.-T. Hsu, J.-K. Huang, C.-L. Hsu, M.-H. Chiu, T. Takenobu, H. Li, C.-I. Wu, W.-H. Chang, A. T. S. Wee, L.-J. Li, Monolayer MoSe₂ grown by chemical vapor deposition for fast photodetection. *ACS Nano* 8, 8582–8590 (2014).
- J.-K. Huang, J. Pu, C.-L. Hsu, M.-H. Chiu, Z.-Y. Juang, Y.-H. Chang, W.-H. Chang, Y. Iwasa, T. Takenobu, L.-J. Li, Large-area synthesis of highly crystalline WSe₂ monolayers and device applications. ACS Nano 8, 923–930 (2014).
- P. J. Zomer, M. H. D. Guimarães, J. C. Brant, N. Tombros, B. J. van Wees, Fast pick up technique for high quality heterostructures of bilayer graphene and hexagonal boron nitride. *Appl. Phys. Lett.* **105**, 013101 (2014).

- W.-T. Hsu, Z.-A. Zhao, L.-J. Li, C.-H. Chen, M.-H. Chiu, P.-S. Chang, Y.-C. Chou, W.-H. Chang, Second harmonic generation from artificially stacked transition metal dichalcogenide twisted bilayers. ACS Nano 8, 2951–2958 (2014).
- N. Kumar, S. Najmaei, Q. Cui, F. Ceballos, P. M. Ajayan, J. Lou, H. Zhao, Second harmonic microscopy of monolayer MoS₂. Phys. Rev. B 87, 161403 (2013).
- L. M. Malard, T. V. Alencar, A. P. M. Barboza, K. F. Mak, A. M. de Paula, Observation of intense second harmonic generation from MoS₂ atomic crystals. *Phys. Rev. B* 87, 201401 (2013).
- Y. Li, Y. Rao, K. F. Mak, Y. You, S. Wang, C. R. Dean, T. F. Heinz, Probing symmetry properties of few-layer MoS₂ and h-BN by optical second-harmonic generation. *Nano Lett.* 13, 3329–3333 (2013).
- A. Raja, L. Waldecker, J. Zipfel, Y. Cho, S. Brem, J. D. Ziegler, M. Kulig, T. Taniguchi, K. Watanabe, E. Malic, T. F. Heinz, T. C. Berkelbach, A. Chernikov, Dielectric disorder in two-dimensional materials. *Nat. Nanotechnol.* 14, 832–837 (2019).
- X. P. Vögele, D. Schuh, W. Wegscheider, J. P. Kotthaus, A. W. Holleitner, Density enhanced diffusion of dipolar excitons within a one-dimensional channel. *Phys. Rev. Lett.* 103, 126402 (2009)
- M. Kulig, J. Zipfel, P. Nagler, S. Blanter, C. Schüller, T. Korn, N. Paradiso, M. M. Glazov,
 A. Chernikov, Exciton diffusion and halo effects in monolayer semiconductors. *Phys. Rev. Lett.* 120, 207401 (2018).
- D. M. Hoffman, G. L. Doll, P. C. Eklund, Optical properties of pyrolytic boron nitride in the energy range 0.05 -10 eV. *Phys. Rev. B* 30, 6051–6056 (1984).
- Y. Li, A. Chernikov, X. Zhang, A. Rigosi, H. M. Hill, A. M. van der Zande, D. A. Chenet, E.-M. Shih, J. Hone, T. F. Heinz, Measurement of the optical dielectric function of monolayer transition-metal dichalcogenides: MoS₂, MoSe₂, WS₂, and WSe₂. *Phys. Rev. B* 90, 205422 (2014).

Acknowledgments

Funding: The spectroscopic experiments performed by J.C. at UT-Austin and X. Li were supported by the Department of Energy, Basic Energy Science program via grant DE-SC0019398. Partial support for K.T. was provided by the NSF MRSEC program DMR-1720595, which also facilitated the collaboration between the group of C.-K.S. and X.L. L.S. and C.-K.S. were supported by the Welch Foundation via grant F-1662 and F-1672. M.S. and K.J. were supported by NSF EFMA-1542747. C.-K.S. acknowledges support from the U.S. Air Force via grant FA2386-18-1-4097. W.-H.C. acknowledges the support from the Ministry of Science and Technology (MOST) of Taiwan (105-2119-M-009-014-MY3 and 107-2112-M-009-024-MY3). W.-T.H. acknowledges the support from the MOST of Taiwan (MOST-107-2917-I-564-010). M.-H.L. and M.-W.C. acknowledge the support from MOST of Taiwan. S.G. and C.-Y.W. acknowledge the support from the MOST of Taiwan (MOST 108-2119-M-007-008). J.Q. acknowledges the support from the China Scholarship Council (grant no. 201706050068). $K.W. \ and \ T.T. \ acknowledge \ support \ from \ the \ Elemental \ Strategy \ Initiative \ conducted \ by \ the$ MEXT, Japan and the CREST (JPMJCR15F3), JST. S.K. was financially supported by the National Research Foundation (NRF) of Korea grant funded by the Korea Government (2017R1D1B04036381). The collaboration between National Tsing-Hua University and The University of Texas at Austin is facilitated by the Global Networking Talent (NT 3.0) Program, Ministry of Education in Taiwan, Author contributions: J.C. and W.-T.H. led the optical experiments. L.S., H.-Y.C., and C.-Y.W. assisted the experiments. J.C. and L.-S.L. led the sample preparations. K.T., M.S., and K.J. assisted in making the samples. T.T. and K.W. provided hBN samples. M.-H.L., W.-T.H., and L.-S.L. performed STEM measurements and analysis. J.Q. and S.K. performed AFM measurements and analysis. J.C., W.-T.H., X.L., and W.-H.C. wrote the manuscript, X.L., M.-W.C., S.G., S.K., C.-K.S., and W.-H.C. supervised the project, All authors discussed the results and commented on the manuscript at all stages. Competing interests: The authors declare that they have no competing interests. Data and materials availability: All data needed to evaluate the conclusions in the paper are present in the paper and/or the Supplementary Materials. Additional data related to this paper may be requested from the authors.

Submitted 13 January 2020 Accepted 6 August 2020 Published 23 September 2020 10.1126/sciadv.aba8866

Citation: J. Choi, W.-T. Hsu, L.-S. Lu, L. Sun, H.-Y. Cheng, M.-H. Lee, J. Quan, K. Tran, C.-Y. Wang, M. Staab, K. Jones, T. Taniguchi, K. Watanabe, M.-W. Chu, S. Gwo, S. Kim, C.-K. Shih, X. Li, W.-H. Chang, Moiré potential impedes interlayer exciton diffusion in van der Waals heterostructures. *Sci. Adv.* 6, eaba8866 (2020).



Moiré potential impedes interlayer exciton diffusion in van der Waals heterostructures

Junho Choi, Wei-Ting Hsu, Li-Syuan Lu, Liuyang Sun, Hui-Yu Cheng, Ming-Hao Lee, Jiamin Quan, Kha Tran, Chun-Yuan Wang, Matthew Staab, Kayleigh Jones, Takashi Taniguchi, Kenji Watanabe, Ming-Wen Chu, Shangjr Gwo, Suenne Kim, Chih-Kang Shih, Xiaoqin Li and Wen-Hao Chang

Sci Adv **6** (39), eaba8866. DOI: 10.1126/sciadv.aba8866

ARTICLE TOOLS http://advances.sciencemag.org/content/6/39/eaba8866

SUPPLEMENTARY http://advances.sciencemag.org/content/suppl/2020/09/21/6.39.eaba8866.DC1 MATERIALS

REFERENCES This article cites 47 articles, 7 of which you can access for free

http://advances.sciencemag.org/content/6/39/eaba8866#BIBL

PERMISSIONS http://www.sciencemag.org/help/reprints-and-permissions

Use of this article is subject to the Terms of Service